Myosin light chain kinase regulates cell polarization independently of membrane tension or Rho kinase

Sunny S. Lou,[1] Alba Diz-Muñoz,[4,5,6,7] Orion D. Weiner,[6,7] Daniel A. Fletcher,[4,5,8] and Julie A. Theriot[2,3]

[1]Department of Chemical and Systems Biology, [2]Department of Biochemistry, and [3]Howard Hughes Medical Institute, Stanford University School of Medicine, Stanford, CA 94305
[4]Department of Bioengineering and [5]Biophysics Program, University of California, Berkeley, Berkeley, CA 94720
[6]Cardiovascular Research Institute and [7]Department of Biochemistry, University of California, San Francisco, San Francisco, CA 94158
[8]Physical Biosciences Division, Lawrence Berkeley National Laboratory, Berkeley, CA 94720

Cells polarize to a single front and rear to achieve rapid actin-based motility, but the mechanisms preventing the formation of multiple fronts are unclear. We developed embryonic zebrafish keratocytes as a model system for investigating establishment of a single axis. We observed that, although keratocytes from 2 d postfertilization (dpf) embryos resembled canonical fan-shaped keratocytes, keratocytes from 4 dpf embryos often formed multiple protrusions despite unchanged membrane tension. Using genomic, genetic, and pharmacological approaches, we determined that the multiple-protrusion phenotype was primarily due to increased myosin light chain kinase (MLCK) expression. MLCK activity influences cell polarity by increasing myosin accumulation in lamellipodia, which locally decreases protrusion lifetime, limiting lamellipodial size and allowing for multiple protrusions to coexist within the context of membrane tension limiting protrusion globally. In contrast, Rho kinase (ROCK) regulates myosin accumulation at the cell rear and does not determine protrusion size. These results suggest a novel MLCK-specific mechanism for controlling cell polarity via regulation of myosin activity in protrusions.

Introduction

Cell migration is important for many biological processes, including development, immunity, and regeneration. To be persistently motile, cells must first polarize to form a single front and rear. Thus, for actin-based motility, the question of how cells establish that single region of actin polymerization and prevent the formation of secondary fronts has been of great interest.

Previous work has largely focused on the role of the small GTPase Rho and its effectors Rho kinase (ROCK) and myosin II. For example, Rho, ROCK, and myosin II inhibition in rapidly motile amoeboid cell types such as *Dictyostelium*, neutrophils, or monocytes results in the conversion of well-polarized single-front cells into cells with multiple competing protrusions (Wessels et al., 1988; Worthylake and Burridge, 2003; Xu et al., 2003), whereas expression of constitutively active Rho or myosin II results in round stationary cells with no protrusions (Xu et al., 2003). Similarly, in slowly moving epithelial and mesenchymal cells, Rho pathway activation decreases protrusion number and vice versa (Wang et al., 2003; Vicente-Manzanares et al., 2007, 2008, 2011; Mseka and Cramer, 2011). There are several proposed mechanisms for how Rho pathway activation inhibits the formation of multiple protrusions. One possibility is that Rho signaling through ROCK directly inhibits the signaling factors that promote actin polymerization (Li et al., 2005; Ohta et al., 2006). Alternatively, downstream activation of myosin II could promote the conversion of branched actin structures to bundles, which cannot accommodate Arp2/3-based branching, thereby locally inhibiting protrusion formation (Vicente-Manzanares et al., 2011).

Recently, multiple studies have shown that membrane tension can also be involved in restricting cells to a single front (Keren et al., 2008; Houk et al., 2012; Lieber et al., 2013). Specifically, artificially increasing tension causes neutrophils to cease protruding (Houk et al., 2012), whereas decreasing tension can induce polarized keratocytes to form multiple lamellipodia (Lieber et al., 2013). In this model, once a single protrusion is formed, the force of actin polymerization pushing on the membrane increases the membrane tension globally, which then mechanically inhibits polymerization elsewhere. However, the

Correspondence to Julie A. Theriot: theriot@stanford.edu

Abbreviations used in this paper: AFM, atomic force microscopy; dpf, days postfertilization; MLCK, myosin light chain kinase; ROCK, Rho kinase.

The Rockefeller University Press $30.00
J. Cell Biol. Vol. 209 No. 2 275–288
www.jcb.org/cgi/doi/10.1083/jcb.201409001

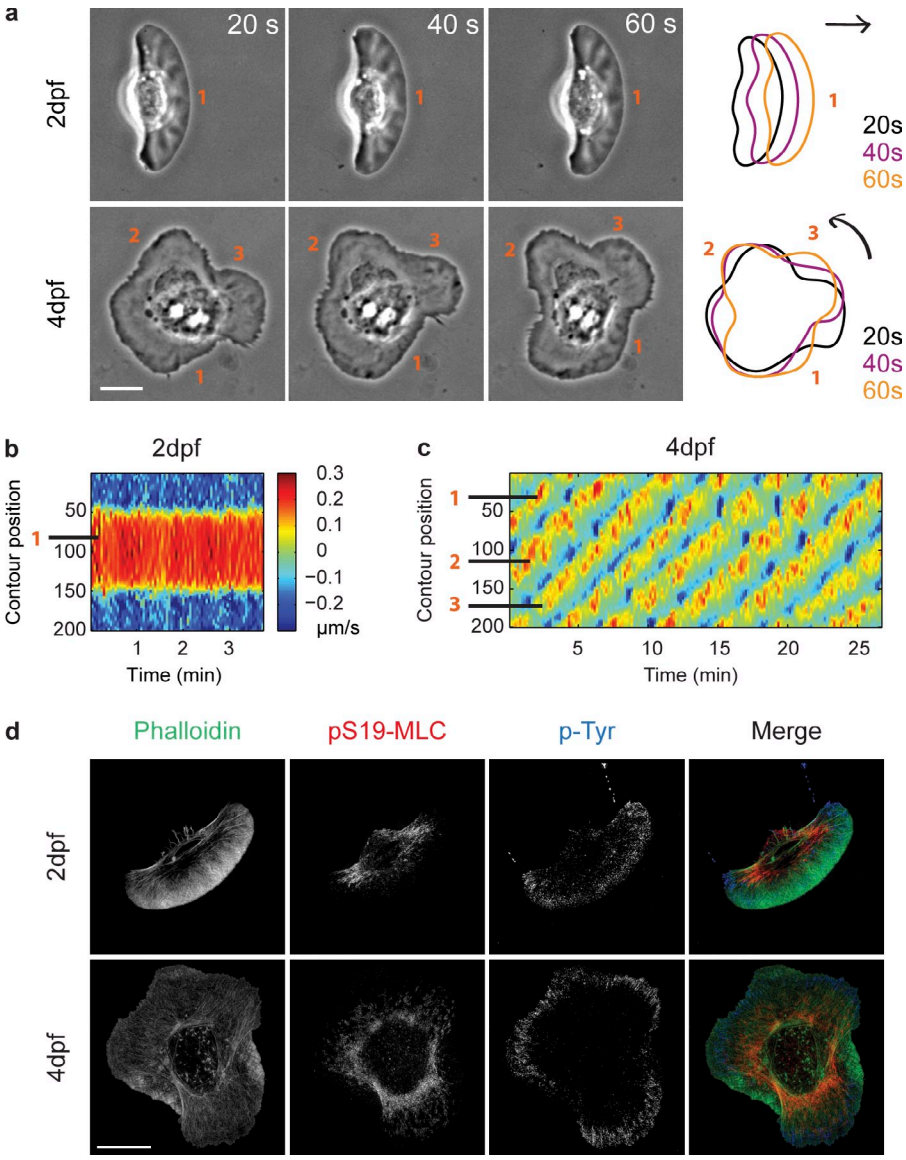

Figure 1. **Zebrafish embryonic keratocytes display different behaviors depending on developmental stage.** (a) Representative images of cells derived from 2-dpf and 4-dpf embryos. Cell outlines are shown on the right. Bar, 10 µm. (b) Typical edge velocity map for a 2-dpf cell, showing one leading edge. Color represents edge velocity, where red is protruding and blue is retracting (see color scale on the right). (c) Typical edge velocity map for a 4-dpf cell, showing three protrusions in this case, which propagate laterally around the cell. (d) Representative immunofluorescence images of 2-dpf and 4-dpf cells. Cells were fixed and stained with AF594-phalloidin to visualize F-actin, a phospho-serine19 myosin light chain antibody to visualize myosin, and a phospho-tyrosine antibody to visualize adhesions. A maximum intensity projection of a z stack acquired using 3D structured illumination microscopy is shown. Bar, 10 µm.

evidence for this model comes from fast-moving cells with strong actin polymerization capable of fully extending the membrane to increase the tension. Whether membrane tension can play a similar role for slow cells with weak protrusions remains less clear.

Furthermore, although there is evidence for both mechanical tension-based and Rho signaling-based mechanisms for establishing cell polarization in fast-moving cells, less is known about the circumstances under which each mechanism is dominant, and it is also not clear whether there are interactions between the signaling and mechanical factors. Fish epithelial keratocytes are an ideal model system for investigating the role of mechanics in cell migration because their simple reproducible cell shapes and cytoskeletal structures have enabled integrated experimental and theoretical approaches, which have resulted in comprehensive whole-cell models incorporating details of molecular interaction with large-scale force balance and protein distribution and transport (Lee et al., 1993; Grimm et al., 2003; Lacayo et al., 2007; Keren et al., 2008; Wilson et al., 2010; Barnhart et al., 2011). However, signaling has been more difficult to study in keratocytes because they are typically cultured from non-genetically tractable species of fish, such as cichlids (Lacayo et al., 2007), goldfish (Lee et al., 1993), or black tetra (Svitkina et al., 1997).

To address these shortcomings, we established a protocol for culturing keratocytes from zebrafish embryos, which have a sequenced genome (Howe et al., 2013) and well-established genetic tools for protein overexpression and knockdown (Lawson and Wolfe, 2011). In this study, we use this system to uncover a surprising role for myosin light chain kinase (MLCK) in regulating cell polarization independent of ROCK and in the context of unchanged membrane tension. Specifically, we find that increased MLCK activity helps keratocytes to form multiple protrusions by increasing myosin accumulation in lamellipodia, thus shortening edge lifetimes and decreasing protrusion size. Our data suggest that ROCK and MLCK regulate spatially distinct populations of myosin, which can have opposing effects on cell polarization.

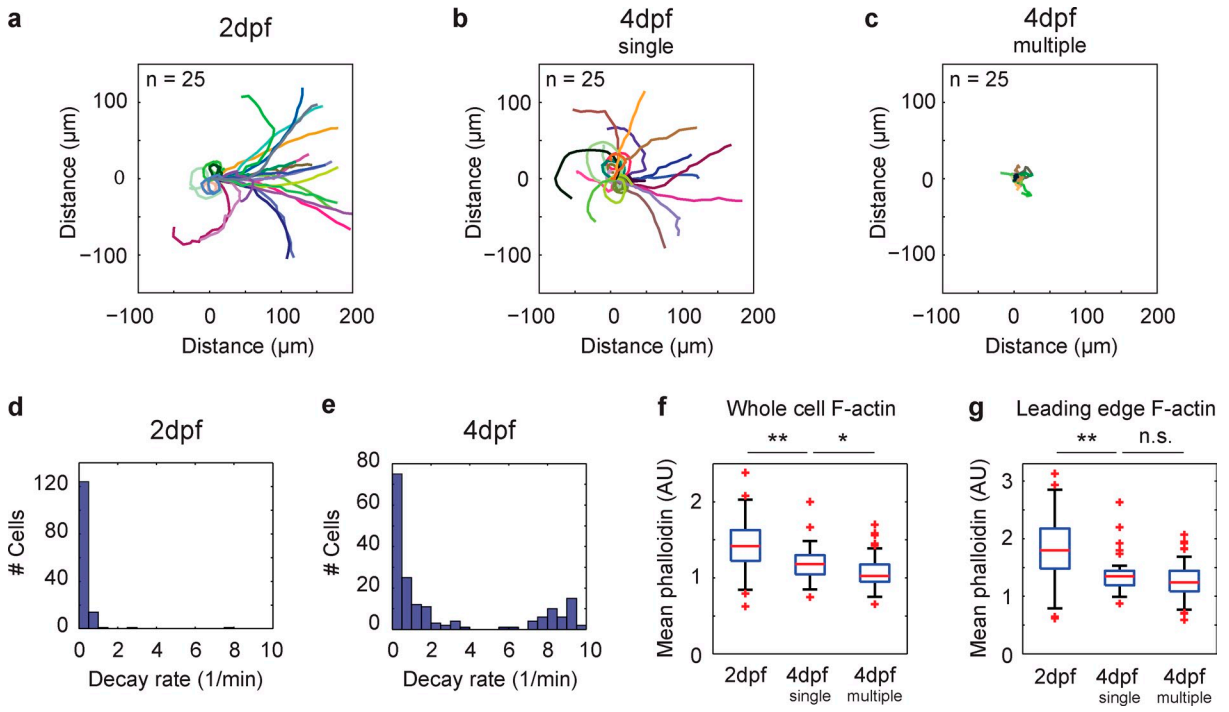

Figure 2. **Single-front and multiple-front 4-dpf cells are drawn from the same population, which is distinct from 2 dpf.** (a–c) Cells from the indicated developmental stage and morphology were tracked for 20 min. 25 randomly chosen tracks are shown. (d and e) Histogram of velocity autocorrelation decay constants for 2-dpf (n = 138) and 4-dpf (n = 177) tracks. Smaller values indicate straighter tracks. (f) Phalloidin intensity, averaged over the entire cell, was measured in 2-dpf (n = 88) and 4-dpf single-front (n = 30) and 4-dpf multiple-front cells (n = 90). (g) Mean phalloidin intensity at the protruding edge was measured in 2-dpf (n = 88) and 4-dpf single-front (n = 30) and 4-dpf multiple-front cells (n = 90). **, $P < 0.01$; *, $P < 0.05$; n.s., $P > 0.05$, as measured by two-sample Wilcoxon rank sum test.

Results

Zebrafish keratocytes display differing behaviors depending on the developmental stage

To culture keratocytes from zebrafish embryos, we needed to develop a new protocol because the standard approach of culturing cells from plucked scales cannot be used in embryos, which do not develop scales until 4 wk postfertilization (Le Guellec et al., 2004). Our most successful protocol uses trypsin to disrupt the embryonic epithelium, and after transferring the supernatant to a fresh surface, typically >90% of the adherent cells are keratocytes. We were able to extract keratocytes from embryonic stages as early as 1 d postfertilization (dpf) and as late as 12 dpf.

However, to our surprise, we observed that zebrafish embryonic keratocytes do not always display the canonical keratocyte shape and behavior that is exhibited by adult keratocytes from other species (Goodrich, 1924; Euteneuer and Schliwa, 1984; Keren et al., 2008). Although cells from 1-dpf and 2-dpf embryos resemble typical adult keratocytes in that they have a single large fan-shaped leading edge and persistent motility, another population of cells emerges starting from 3 dpf onwards that appear to have multiple leading edges that travel laterally around the cell (Fig. 1 a and Video 1). We will take the 2-dpf and 4-dpf cell populations as representative time points for the remainder of this study.

To characterize the difference in protrusion dynamics between the single-front and multiple-front cells, we measured edge protrusion and retraction velocities at all points around the cell's perimeter. Single-front cells have a single protruding and retracting edge (Fig. 1 b) and accordingly are polarized along a single front-back axis. Multiple-front cells, however, do not simply protrude at random points around the perimeter, but instead show a consistent pattern of regularly spaced protrusions that propagate circumferentially (Fig. 1 c) and can be stable for hours, which suggests that these cells are not simply unpolarized but rather are polarized along multiple front–back axes. We also examined the organization of F-actin, myosin, and adhesions in these two populations using immunofluorescence (Fig. 1 d).

To determine if cells with multiple protrusions have poor net translocation efficiency, we tracked 2-dpf and 4-dpf cells over the course of 20 min (Fig. 2, a–c). While 2-dpf cells can translocate distances of up to 200 μm in that time, typically >40% of 4-dpf cells are multiple-front cells and correspondingly are not able to move >40 μm. To quantify persistence, we calculated the velocity autocorrelation function for individual tracks. As expected of persistent cells, all 2-dpf tracks exhibited slow decay of the velocity autocorrelation (Fig. 2 d). However, the autocorrelation for 4-dpf tracks decayed much faster (Fig. 2 e), with both an increase in turning single-front cells as well as relatively stationary multiple-front cells. Therefore, despite their close relation in developmental time, 2-dpf cells and 4-dpf cells self-organize to very different polarity states that have functional consequences for their motility abilities. We were interested in understanding the mechanisms underlying differential regulation of cell polarity in 2-dpf and 4-dpf cells.

However, because single-front cells persist in the 4-dpf population, it was not clear if the multiple-front 4-dpf cells represent a distinct subpopulation with different molecular properties from all single-front cells, or if instead the 4-dpf population as a whole expresses different components that allow for stochastic emergence of the multiple-front phenotype. To distinguish between these two possibilities, we quantified the mean density of F-actin present throughout the whole cell in 2-dpf and 4-dpf single-front and 4-dpf multiple-front cells (Fig. 2 f), and found that 4-dpf single-front cells have a lower mean F-actin density than 2-dpf cells. Furthermore, 2-dpf cells have higher F-actin density at the leading edge as compared with both types of 4-dpf cells, which are indistinguishable using this metric (Fig. 2 g). 4-dpf single-front cells also turn more as compared with 2-dpf single-front cells (Fig. 2, d and e). These data suggest that both phenotypes of 4-dpf cells are drawn from the same population. Most importantly, we sometimes observe spontaneous conversion of single-front 4-dpf cells to the multiple-front phenotype, and vice versa. Therefore, understanding the origin of the multiple-front state is equivalent to understanding the phenotypic differences in motility between the 2-dpf and 4-dpf populations.

Intrinsically small protrusions enable 4-dpf cells to have multiple fronts

Previous work has established the essential role for membrane tension in globally limiting protrusion size and restricting keratocytes to a single front (Keren et al., 2008; Lieber et al., 2013). Therefore, we sought to test whether the multiple-front state was caused by 4-dpf cells having too low a membrane tension to suppress secondary protrusions, as had been previously reported to occur after a sudden decrease in membrane tension caused by fusion of membrane vesicles to polarized cells (Lieber et al., 2013). We used atomic force microscopy (AFM) to pull membrane tethers from keratocytes and measured membrane tension from the tether rupture force (Fig. 3 a; Materials and methods). However, we found that membrane tension is unchanged between 2-dpf and 4-dpf single-front and 4-dpf multiple-front cells (Fig. 3 b), thus raising the possibility that, although membrane tension may globally limit protrusion, other factors might locally regulate the intrinsic size of individual fronts and permit the coexistence of multiple fronts under the global limit set by membrane tension. Alternatively, protrusion size in the 4-dpf cells could be limited by competition between the multiple fronts.

We find that protrusions in 4-dpf multiple-front cells are 22 ± 4 µm (SD), whereas protrusions in 2-dpf cells are 34 ± 5 µm (SD; Fig. 3 c). To determine whether the protrusions in 4-dpf cells are intrinsically small rather than small due to competition, we removed all the protrusions by depolymerizing the F-actin with DMSO (Keren et al., 2008), and observed whether upon washout cells could make larger protrusions in the absence of other potentially competing protrusions. Cells tended to make a single protrusion first after DMSO washout, followed by the formation of additional protrusions (Fig. 3 d and Video 2). We quantified the size of the first protrusion that formed after washout and found it to be comparable to the mean size of the protrusions before perturbation (Fig. 3, e and f). In contrast, in the same experiment, 2-dpf cells will immediately make a single protrusion that grows to become a large front (Fig. 3 d and Video 2). Consistent with the idea that protrusions in 4-dpf multiple-front cells have a limited intrinsic size, we found that protrusion width is independent of cell size in this population (Fig. S2 d); larger cells typically have more protrusions rather than bigger ones (Fig. S2 e). Therefore, we conclude that 4-dpf cells are able to have multiple protrusions because their protrusions are intrinsically small.

Protrusion lifetime and lateral propagation rate determine protrusion size

To understand why 4-dpf cells have smaller protrusions, we sought to identify how protrusion width is determined. In single-front cichlid keratocytes, it has previously been shown that membrane tension and the ratio of Arp2/3-mediated branching to capping regulates protrusion width (Lacayo et al., 2007; Keren et al., 2008; Ofer et al., 2011). However, this mechanism seems unlikely in multiple-front cells if membrane tension is not regulating local protrusion size. Indeed, treatment with the Arp2/3 inhibitor CK666 (Nolen et al., 2009) had no effect on protrusion width (Fig. S2 c), despite resulting in clear changes in F-actin organization (Fig. S2, a and b), which suggests that the branching-to-capping ratio is not the main determinant of protrusion width in this case.

Because 4-dpf multiple-front cells have traveling waves of protrusion, we speculated instead that the dynamics of protrusion could regulate edge width. Specifically, edge width should be the product of edge lifetime, i.e., the duration of time each region of edge remains protrusive, and the lateral propagation rate (Fig. S1 e). Although edge width is correlated with edge lifetime and weakly correlated with lateral propagation (Fig. S3, a and b), the product of lifetime and lateral propagation rate provides a much better prediction of width than either correlation on its own (Fig. 3 g), which suggests that the combination of edge lifetime and lateral propagation rate determine protrusion width in 4-dpf cells.

Increased MLCK expression in 4dpf cells largely explains the multiple-front phenotype of 4-dpf cells

We hypothesized that these differences in protrusion dynamics observed between 2-dpf and 4-dpf cells might be driven by underlying changes in expression of cytoskeletal structural proteins and regulators. We used RNAseq to measure changes in expression of cytoskeleton-related genes between 2 dpf and 4 dpf, and found only six such genes whose expression was significantly different (Fig. 4 a). Two of these hits, *arpc5a* and *flnb*, represent minor isoforms with a close paralogue expressed at much higher levels and thus seemed to be unlikely candidates. *tnw* is a secreted extracellular matrix protein and seemed unlikely to contribute because the multiple-front phenotype is observed when cells are cultured on a fresh glass surface. Two hits, *gsnb* and *scinla*, are both gelsolin members that are less expressed at 4 dpf. However, microinjection of purified gelsolin into 4-dpf cells had no effect (unpublished data). That left us with one particularly interesting

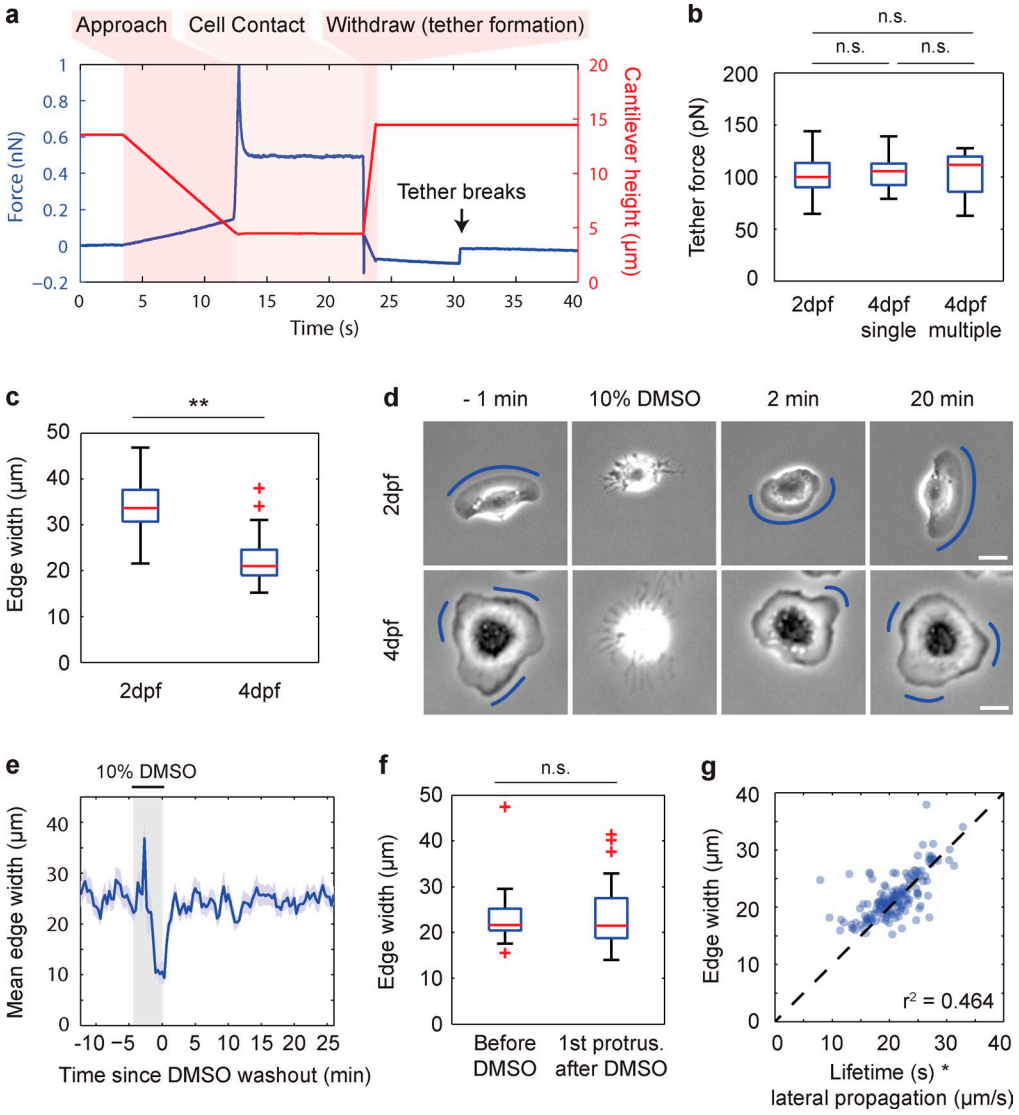

Figure 3. **4-dpf cells have multiple protrusions because the protrusions are intrinsically small.** (a) Example force–time curve showing a membrane tether force quantification. A concanavalin A–coated AFM cantilever is brought into contact with the cell for 10 s and then withdrawn. At this time, a membrane tether connecting the cell to the cantilever produces a negative force reading. After tether breakage, the force experienced by the cantilever returns to zero. The difference between the prebreakage and postbreakage force is quantified as the tether force. (b) Tether force was measured in 2-dpf (n = 25) and 4-dpf single-front (n = 8), and 4-dpf multiple-front (n = 15) cells. n.s., $P > 0.05$ as measured by a two-sample t test. (c) Mean protrusion width measured in individual 2-dpf (n = 61) and 4-dpf (n = 157) multiple-front cells. **, $P < 0.01$ as measured by a two-sample Wilcoxon rank sum test. (d) A representative 2-dpf single-front cell (top) or 4-dpf multiple-front cell (bottom) treated with 10% DMSO to depolymerize F-actin. Time shown in minutes before/after DMSO addition/washout. Images are representative of 2-dpf (n = 12) and 4-dpf (n = 35) cells. Blue lines indicate protrusions. Bars, 10 µm. (e) Mean protrusion width before and after DMSO washout as measured in individual 4-dpf multiple-front cells (n = 35). The gray shaded region indicates the duration of DMSO treatment. The blue shaded region represents standard error. (f) The mean width of protrusions before DMSO addition, and width of the first protrusion after DMSO washout were measured in individual cells (n = 35). n.s., $P > 0.05$, paired-sample t test. (g) Mean edge width plotted against the product of mean edge lifetime and mean lateral propagation rate for individual 4-dpf multiple-front cells (n = 154). The broken line is y = x.

candidate: *im:7148400*, the only MLCK isoform expressed in zebrafish embryonic keratocytes. *im:7148400* is expressed about twofold more highly in 4-dpf cells as compared with 2-dpf cells, as confirmed by qRT-PCR (Fig. 4 b).

To test whether increased MLCK activity in 4-dpf cells is important for the multiple-front phenotype, we treated 4-dpf cells with ML7, a small molecule inhibitor of MLCK (Saitoh et al., 1987). 25 µM ML7 converted ~50% of multiple-front cells to a single front phenotype (Fig. 4 c and Video 3). BATI, a peptide inhibitor of MLCK (Totsukawa et al., 2004), had a similar effect (Fig. 4 c). To confirm that an increase in im:7148400 expression specifically is responsible for the multiple front phenotype, we designed a morpholino to induce mis-splicing and early termination of the im:7148400 transcript (Fig. 4 d). 4-dpf keratocytes from morpholino-injected embryos also displayed a higher percentage of single-front cells in the population as compared with mock-injected control (Fig. 4 d). Therefore, increased MLCK expression in 4-dpf keratocytes contributes to allowing the formation of multiple fronts. To determine whether MLCK might be specifically regulating a particular isoform of myosin II, we also compared expression levels of myosin IIa, IIb, and IIc, and found that nearly all (>98%) of detectable

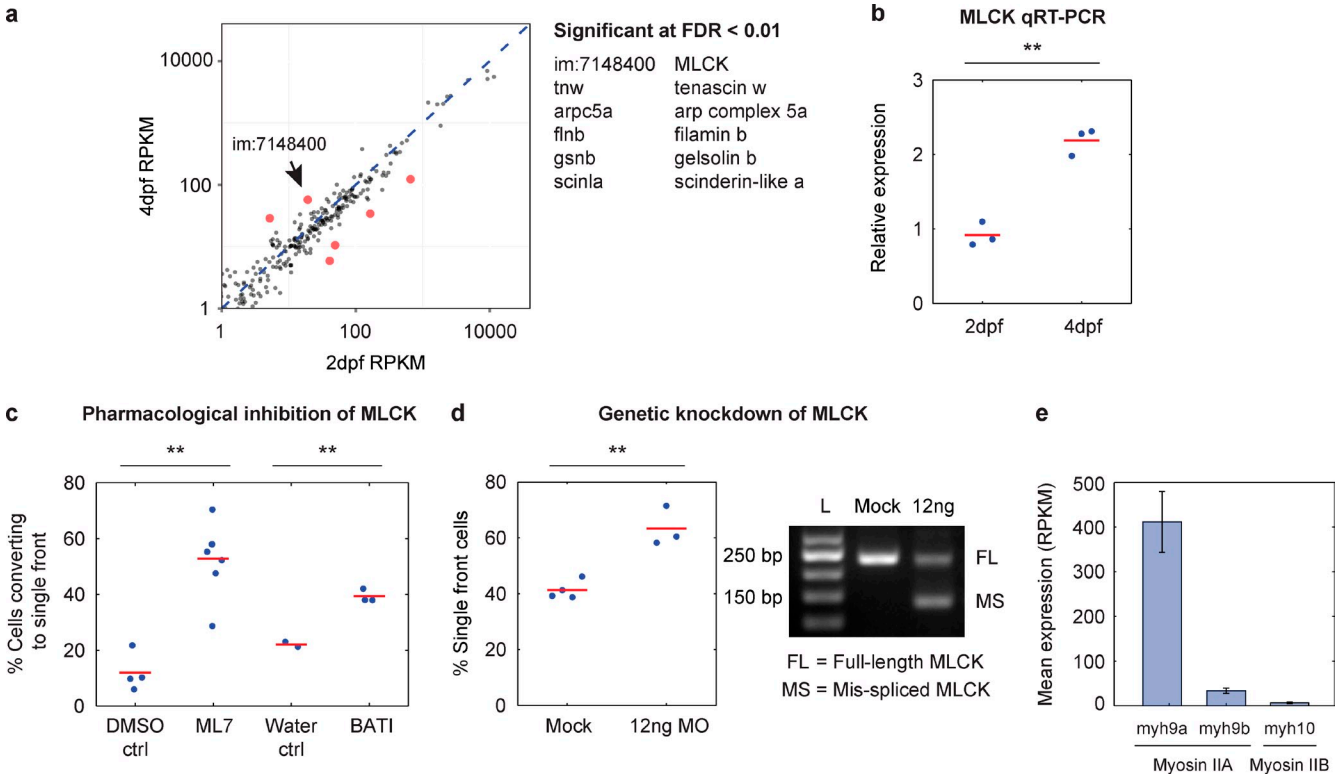

Figure 4. **Increased MLCK expression in 4-dpf cells is largely responsible for the multiple-front phenotype.** (a) Expression of cytoskeleton-related genes as measured in 2-dpf and 4-dpf cells by RNAseq. Each dot represents the mean expression level of one cytoskeleton-related gene over three biological replicates for each developmental stage. Genes highlighted in red were differentially expressed at a false discovery rate (FDR) <0.01. The broken line indicates y = x. (b) Expression of im:7148400 measured in 2-dpf and 4-dpf cells by qPCR and shown normalized to the expression level in 2-dpf cells. Points represent biological replicate measurements; red bars represent means. (c) Conversion of 4-dpf multiple-front cells to a single-front phenotype after treatment with MLCK inhibitors. 4-dpf multiple-front cells were treated with DMSO control, 25 µM ML7, water control, or 20 µM BATI. Each dot represents an independent experiment. At least 180 cells were scored in total for each condition. (d) The effect of MLCK morpholino on 4-dpf cell behavior. Left, percentage of single-front cells in the 4-dpf keratocyte population. Each dot represents a single coverslip. At least 300 cells were scored for each condition. Data shown are from a single batch of injections and are representative of four injection batches. Right, morpholino-induced splicing changes as measured by PCR in individual 4-dpf embryos. L indicates a 50-bp ladder. (e) Expression of myosin isoforms as measured by RNAseq, plotted as reads per kilobase per million mapped (RPKM). Data shown were pooled from three replicates each of the 2-dpf and 4-dpf cells. Error bars indicate standard error of the mean. Myosin IIC was not detectable. **, P < 0.01 as measured by two-sample *t* test.

myosin II transcripts in these cells encode myosin IIa (Fig. 4 e); furthermore, the relative expression level of the isoforms does not change significantly between 2 dpf and 4 dpf.

Decreasing MLCK activity in 4-dpf cells results in longer edge lifetimes and wider edges

Because small protrusions allow 4-dpf cells to make multiple fronts, we wondered whether MLCK inhibition was enabling whole-cell polarization by increasing protrusion size. Therefore, we looked at the dynamics of how ML7 treatment converts multiple-front cells to the single-front phenotype (Fig. 5 a). From the edge velocity map for the representative cell shown, it appears that protrusion width increases shortly after ML7 treatment. To confirm this, we measured mean edge width in a larger population of cells before and after ML7 treatment and found that width does indeed increase upon MLCK inhibition (Fig. 5 b). Because edge width can be regulated by both edge lifetime and the lateral propagation rate, we wondered which of these two parameters is regulated by MLCK activity. Upon MLCK inhibition, we do not observe a change in the lateral propagation rate (Fig. 5 c), but we do observe an increase in edge lifetime (Fig. 5 d), which suggests that MLCK activity regulates edge size by controlling edge lifetime. The effect of ML7 on edge lifetime and not the lateral propagation rate is also visible in individual cell edge velocity maps (Fig. 5 a).

Furthermore, polarization to the single-front state could conceivably happen either by the cells first forming a single large rear, or by forming a large front, as is suggested by the edge lifetime hypothesis. Because MLCK activity could potentially also regulate the strength of the rear by enhancing myosin bundling or contractility, we wanted to exclude the possibility that the mechanism of polarization is driven by changes in rear size rather than front size. Therefore, we measured the size of the largest protruding and retracting section in cells immediately after addition of ML7 (Fig. 5 e). Consistent with our proposal that MLCK activity primarily regulates front size, we see an increase in front size preceding an increase in rear size with a time lag of ∼60 s. Thus, MLCK regulates cell polarity by first modulating front size and number, rather than rear size.

Because we had previously shown that 2-dpf cells have higher F-actin density at the leading edge than 4-dpf cells

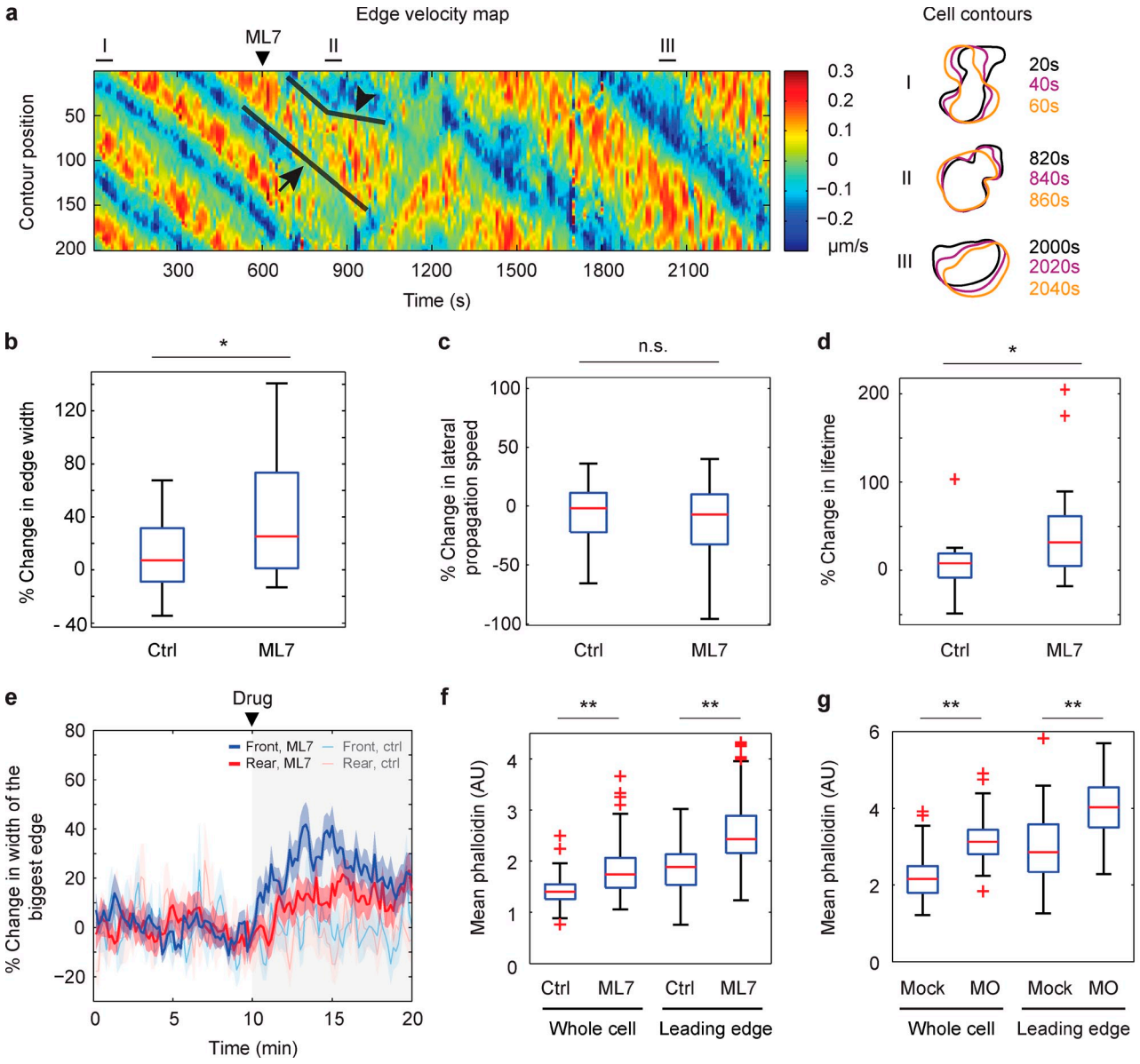

Figure 5. **Decreased MLCK activity causes bigger protrusions by increasing edge lifetime.** (a) Representative edge velocity map (left) and cell contours sampled at the indicated times (right) for a 4-dpf multiple-front cell treated with 25 μM ML7 at the indicated time. The arrow indicates little change in the lateral propagation rate after drug addition. The arrowhead indicates prolonging of edge lifetime after drug addition, resulting in increased protrusion width. Data are representative of 33 independent experiments. (b–d) Mean protrusion width, lateral propagation speed, and edge lifetime measured in individual 4-dpf cells before and after DMSO control (n = 14) or 25 μM ML7 treatment (n = 33). (e) Mean change in the size of the largest protruding region and the largest retracting region in individual 4-dpf cells over time as normalized to their respective sizes before drug treatment. Shaded regions show standard error. (f and g) Change in F-actin density after MLCK inhibition. 4-dpf cells either treated with DMSO control (n = 155) or drug (n = 149) for 15 min (f) or derived from mock (n = 72) or morpholino-injected embryos (n = 79; g) were fixed and stained with 0.2 μM Texas Red-X phalloidin. Mean phalloidin intensity is shown quantified in either the entire cell or only at leading edges. **, $P < 0.01$; *, $P < 0.05$; n.s., $P > 0.05$ as measured by a two-sample Wilcoxon rank sum test.

(Fig. 2 g), we also measured F-actin density in 4-dpf cells 15 min after ML7 addition and found a significant increase in F-actin density both at the leading edge and throughout the cell (Fig. 5 f). In fact, long-term MLCK inhibition via morpholino injection rescues the F-actin amount in 4-dpf cells back to 2-dpf levels (Fig. 5 g). However, although the population distribution of F-actin in these cells fully overlaps with that of 2-dpf cells, some multiple-front cells persist in the population (Fig. 4, c and d), which suggests that rescuing F-actin alone is not sufficient to convert all multiple-front cells.

MLCK regulates myosin accumulation in lamellipodia

To understand how increased MLCK expression in 4-dpf cells regulates edge lifetime, we examined the dynamics of myosin localization in multiple-front cells. Fluorescently tagged myosin appears to incorporate rapidly into the growing lamellipodial actin network and can be found increasingly closer to the leading edge as it switches from protrusion to retraction (Fig. 6 a and Video 4). Because new myosin minifilaments preferentially associate with existing bound filaments (Verkhovsky

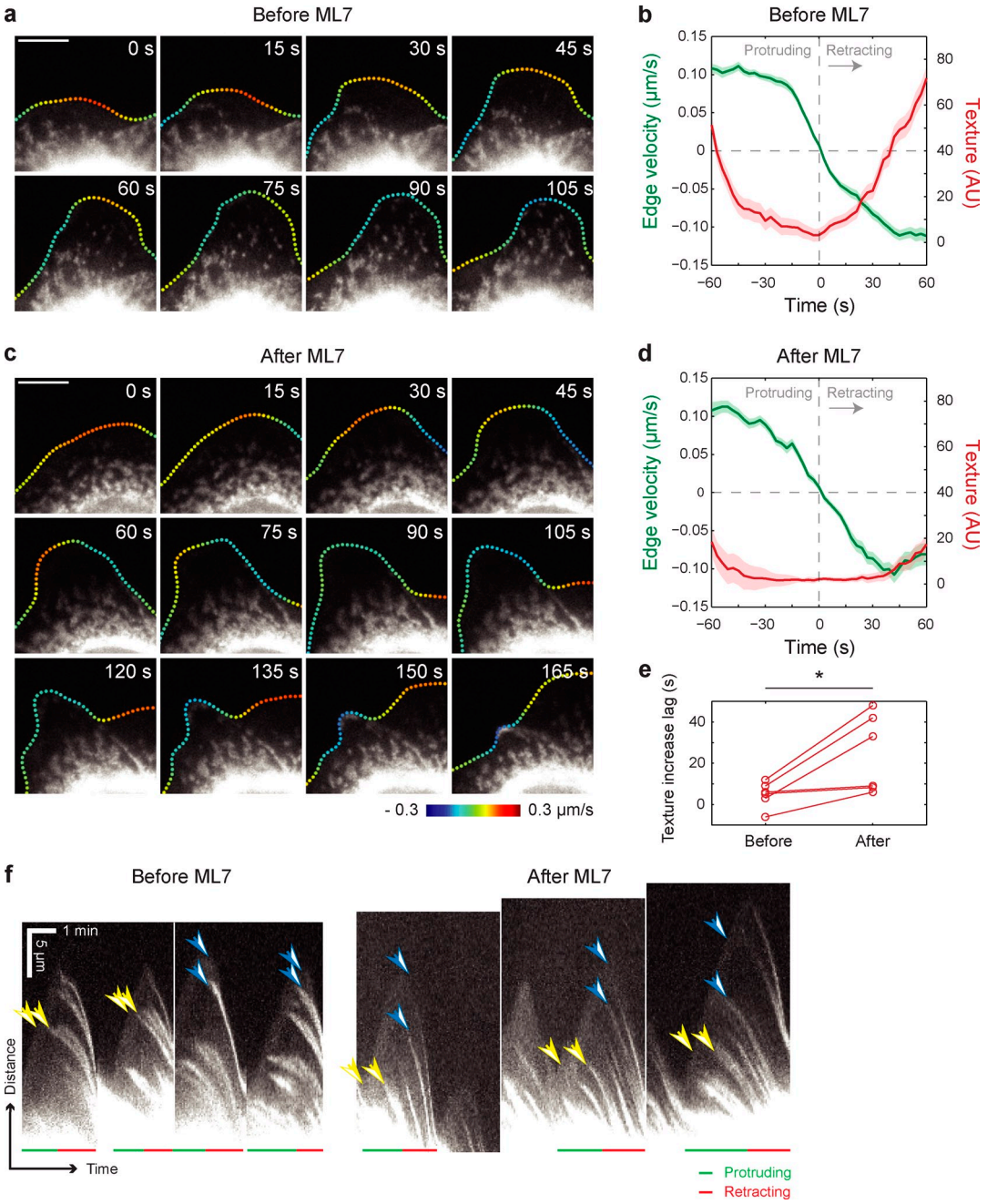

Figure 6. **Myosin accumulates more slowly in protrusions after MLCK inhibition.** (a and c) Images of mApple-myosin light chain dynamics in a representative 4-dpf cell before (a) and 2 min after 25 µM ML7 addition (c). The cell edge is represented by a series of colored dots, where color indicates the velocity of each region of the edge. Red is protruding, blue is retracting (see scale at the bottom). Bars, 10 µm. (b and d) Myosin accumulation behind the leading edge over time quantified in the representative cell shown in a and c, using an image texture score (see Materials and methods) before (b) and 2–5 min after (d) addition of ML7. Measurements were made at 200 regions around the cell perimeter and aligned to the onset of retraction for each protrusion–retraction cycle. Mean protrusion velocity and texture are shown. Shaded regions indicate standard error. (e) Time lag between retraction onset and onset of myosin texture increase as measured in 4-dpf cells before and after addition of 25 µM ML7 ($n = 6$). *, $P < 0.05$ as measured by a paired-sample *t* test. (f) Kymographs taken from the cell shown above. Yellow arrows show that myosin takes a longer time to accumulate in protrusions after ML7 treatment. Blue arrows show that myosin often is localized further away from the protrusion tip after ML7 treatment. Red and green lines indicate duration of protrusion (red) and retraction (green).

et al., 1995; Svitkina et al., 1997; Burnette et al., 2014), the appearance of fluorescently labeled myosin in the lamellipodium is highly nonuniform, with a pronounced and measurable texture. Thus, to quantify the dynamics of myosin accumulation, we measured the amount of myosin fluorescence texture in the region behind the leading edge as the edge underwent cycles of protrusion and retraction. We found that the myosin accumulation immediately behind the leading edge was very well correlated with the onset of retraction (Fig. 6 b), and kymograph analysis of myosin fluorescence shows that myosin can be found throughout the lamellipodium preceding retraction (Fig. 6 f).

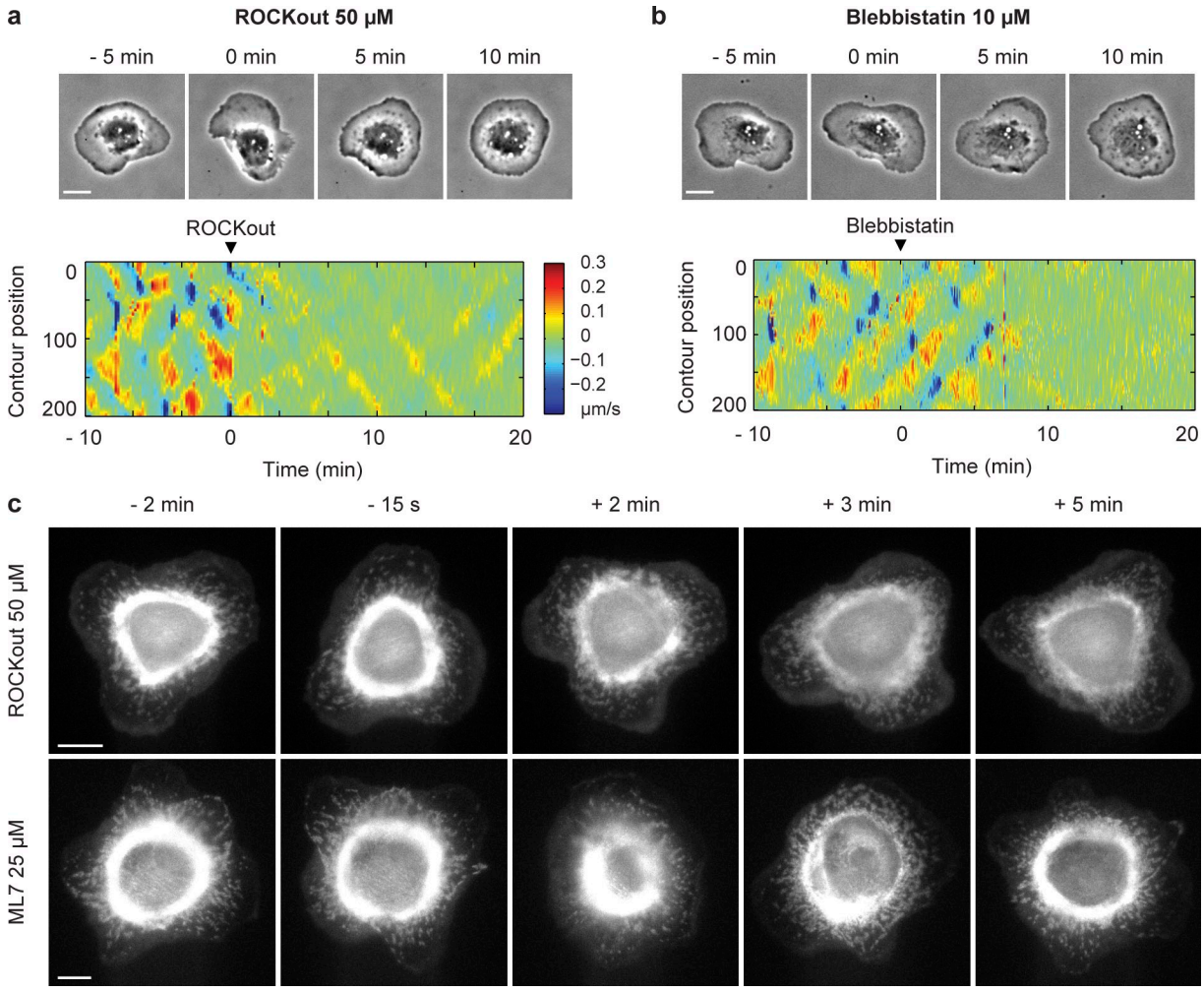

Figure 7. **ROCK and MLCK have spatially distinct roles.** (a and b) Images (top) and edge velocity map (bottom) of a representative 4-dpf cell before and after treatment with 50 µM ROCKout (a) or 10 µM blebbistatin (b). Arrowheads indicate the time of drug addition. (c) Images of mApple-myosin light chain distribution in a representative 4-dpf cell before and after treatment with ROCKout (top) or ML7 (bottom). Bars, 10 µm. Indicated times are relative to the time of drug addition.

If myosin accumulation in protrusions were responsible for edge retraction, we should expect that in the presence of ML7, where edge lifetimes are prolonged, myosin accumulation behind the leading edge would be delayed. Therefore, we measured the rate of myosin accumulation in cells before and after ML7 treatment, and found a significant delay in the onset of myosin accumulation (Fig. 6, c–e; and Video 5) after drug addition. Furthermore, kymograph analysis of myosin fluorescence confirms that myosin seems to accumulate more slowly and further away from the leading edge after MLCK inhibition (Fig. 6 f). These data are consistent with the idea that MLCK regulates edge lifetime and protrusion size by controlling the amount of myosin found in lamellipodia.

ROCK regulates myosin localization at the cell rear

Because ROCK and MLCK both regulate myosin phosphorylation, we wondered whether the effects of MLCK on cell polarization were specific to MLCK or if they might simply reflect overall myosin phosphorylation or activation state. Therefore, we treated 4-dpf cells with the ROCK inhibitor ROCKout (Yarrow et al., 2005) and observed that rather than converting multiple-front cells to a single front, it instead caused the cells to become round and less protrusive (Fig. 7 a). Similar effects were seen with the myosin ATPase inhibitor blebbistatin (Fig. 7 b). Note that the ROCK inhibitor Y-27632 had no phenotype (Fig. S4), and has previously been reported to be ineffective in zebrafish (Weiser and Kimelman, 2012).

The differing effects of ROCK and MLCK inhibition suggested that the two kinases might regulate spatially distinct populations of myosin. In multiple-front keratocytes, the majority of myosin is localized in a ring around the cell body (Fig. 1 d). This actin- and myosin-rich ring is similar to the bundle of actomyosin filaments that form the rear of single-front keratocytes. Upon ROCK inhibition, myosin localization in this central ring decreases dramatically (Fig. 7 c). In contrast, upon MLCK inhibition, myosin intensity in the central ring tends to increase as the ring appears to constrict, followed by reequilibration to a state similar to pre-perturbation (Fig. 7 c). Furthermore, ROCK inhibition has no effect on protrusion width or lifetime

despite causing a decrease in protrusion speed (Fig. S5, a–c), and the rate of myosin accumulation in lamellipodia may in fact be slightly increased (Fig. S5, d and e), perhaps due to more myosin being available for MLCK to phosphorylate. These results suggest that ROCK is primarily responsible for myosin localization to the central ring, which is equivalent to the cell rear in single-front keratocytes and other cell types, whereas MLCK is responsible for myosin localization in lamellipodia at the cell front.

Discussion

Here, we identify a novel mechanism for limiting protrusion size and overall cell polarity by describing a surprising shift in keratocyte behavior from the canonical fan-shaped cell found in adult skin as well as in 2-dpf embryos to a multiple-front traveling wave phenotype seen at 4 dpf. Using the genetic tools available in zebrafish embryos, we identify MLCK as a key regulator of this phenotypic switch, where increased MLCK expression in keratocytes derived from 4-dpf embryos results in more myosin accumulation in lamellipodia, thus shortening the duration of time that edges remain protrusive and causing protrusions to be intrinsically small, which allows for the formation of multiple protrusive fronts.

The mechanism for MLCK-driven lamellipodial myosin accumulation to decrease edge lifetime could either be actin depolymeriztion (Murrell and Gardel, 2012; Vogel et al., 2013) or direct force on the meshwork, sweeping it backward toward the center of the cell (Ponti et al., 2004; Cai et al., 2006; Barnhart et al., 2011). In this model, edge lifetime is determined by whether actin polymerization can outrun myosin accumulation. It has previously been shown that myosin and MLCK activity can trigger retraction and shorten edge lifetimes (Giannone et al., 2004; Burnette et al., 2011; Tsai and Meyer, 2012) in other cell types, including fibroblasts, epithelial cells, and endothelial cells. It is important to note though that in 4-dpf keratocytes, edge retraction still occurs after MLCK inhibition (Fig. 6, c and d). Because myosin is still present in the central ring after ML7 treatment, it is possible that retraction is still occurring due to myosin-driven contractility of the actin meshwork acting at a distance. However, it has also been reported at least in PtK1 cells that protrusion and retraction cycles still occur after complete myosin II inhibition (Burnette et al., 2011). It seems likely that there are other factors such as actin-depolymerizing proteins (Wilson et al., 2010; Mseka and Cramer, 2011) that contribute to retraction in addition to myosin.

Our results show that MLCK facilitates the multiple-front state and thus inhibits overall cell polarization by locally suppressing the size of individual protrusions (Fig. 5). Membrane tension has previously been shown in keratocytes and neutrophils to promote cell polarization by acting as a global inhibitor of protrusion (Keren et al., 2008; Houk et al., 2012; Lieber et al., 2013). In this model, once a single large front is formed, it pushes on the membrane to increase overall tension, which mechanically suppresses the formation of other protrusions. Notably, we show that the multiple fronts found in 4-dpf cells are not caused by low membrane tension as has previously been shown when the total membrane amount is suddenly increased (Lieber et al., 2013), as membrane tension is the same at 2 dpf and 4 dpf (Fig. 3 b). Instead, we propose that tension could be playing a role in limiting the number of protrusions by acting as a global inhibitor of polymerization. Because tension is set by cytoskeletal forces (Lieber et al., 2013) and because MLCK causes 4-dpf cells to have intrinsically small protrusions, perhaps each protrusion alone does not increase the membrane tension enough to suppress others, so the cells continue to make protrusions until the total tension reaches an inhibitory level. We speculate that membrane tension could be playing a role in suppressing protrusion number in other slow-moving cell types with small protrusions, but that it is only capable of driving cell polarization when the protrusions are large and strong as in fast-moving cell types like adult keratocytes and neutrophils.

Additionally, we find that MLCK regulates cell polarity independently of ROCK. While MLCK appears to control myosin accumulation in lamellipodia (Fig. 6), ROCK instead regulates myosin localization to the central actin bundle (Fig. 7), which is a structure analogous to the actin bundles that define the rear of other cell types (Wilson et al., 2010; Vicente-Manzanares et al., 2011). These results are consistent with previous literature describing the role for MLCK in regulating myosin phosphorylation specifically in lamellipodia while ROCK is instead responsible for controlling the level of myosin phosphorylation in the central regions of the cell (Chew et al., 2002; Totsukawa et al., 2004). MLCK is also localized to the leading edge of neutrophils (Xu et al., 2008), whereas Rho activity is localized to the rear (Wong et al., 2006).

These distinct spatial roles likely explain the discrepancy between our results and the literature describing the role of myosin in cell polarity (Fig. 8). Specifically, while we describe how increased MLCK and myosin activities enable the formation of multiple fronts and how low myosin activity is necessary for the single-front state, the canonical view is that excess myosin activity results in stationary cells that are nonprotrusive, and myosin inhibition results in cells that have multiple fronts (Wessels et al., 1988; Wang et al., 2003; Xu et al., 2003; Totsukawa et al., 2004; Yam et al., 2007; Vicente-Manzanares et al., 2008, 2011; Mseka and Cramer, 2011). However, these previous results all focused on the role of Rho/ROCK-dependent myosin contractility in helping cells build a stable rear that inhibits protrusion. Even in adult keratocytes, polarization from the stationary to single-front state requires that the cells first establish a region of retraction driven by myosin contractility, which requires ROCK signaling but not MLCK (Yam et al., 2007).

We propose that MLCK is responsible for a separate mechanism for cell polarization by acting at the cell front to regulate protrusion size directly. Furthermore, our finding that MLCK-dependent myosin inhibition can promote cell polarization is consistent with observations in other cell types. For example, myosin inhibition in normally stellate embryonic stem cells and fibroblasts can induce the formation of a keratocyte-like large single-front morphology (Even-Ram et al., 2007; Cai et al., 2010), and myosin knockdown in a mouse model of squamous cell carcinoma increased tumor cell motility and invasiveness (Schramek et al., 2014), which suggests that this

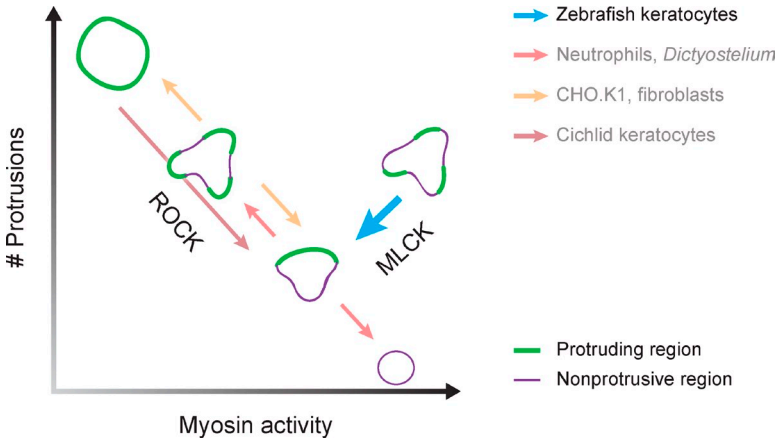

Figure 8. **MLCK and ROCK can independently regulate cell polarization.** The Rho–ROCK–myosin pathway has previously been found to play a role in regulating large-scale cell polarity by acting at the cell rear, such that decreasing myosin activity increases the protrusion number. We propose that a MLCK–myosin pathway can also regulate cell polarity by acting at the cell front to directly control protrusion lifetime and size. Our results show that decreasing MLCK activity decreases protrusion number.

MLCK-dependent cell polarization mechanism may generalize to other motile cells. Furthermore, even in cells like neutrophils that use Rho- or membrane-tension–mediated polarization mechanisms, MLCK activity at the leading edge could still contribute to protrusion morphology or dynamics.

Finally, the 4-dpf multiple-front cells are notable in having protrusions with remarkably regular spacing and propagation (Fig. 1). Traveling waves of protrusion have been observed in many cell types (Machacek and Danuser, 2006) and have recently been a topic of increasing interest (Ryan et al., 2012; Allard and Mogilner, 2013). In the framework of traveling waves, our results indicate that MLCK can regulate wave termination. We speculate that the regular spacing of protrusions reflects the fact that a new protrusion cannot begin until a retraction has completely finished; i.e., the accumulation of myosin in retracting regions provides a refractory period to protrusion. The mechanism underlying lateral propagation of the protrusions is less clear, but the typical rate of propagation (~0.2 µm/s) is consistent with the diffusion of a membrane-bound regulator. The details of how 4-dpf keratocytes generate such striking traveling waves would be an interesting topic for future exploration.

Materials and methods

Cell culture and reagents

Wild-type zebrafish (TL strain) were maintained and embryos were collected according to standard procedures (Westerfield, 2007). For keratocyte extraction, dechorionated zebrafish embryos were washed twice with PBS and incubated at 4°C in cell dissociation buffer (Invitrogen) for 30 min. Embryos were then transferred into 0.25% trypsin + 1 mM EDTA (Invitrogen) for 10 min at 28°C. Trypsin activity was quenched by the addition of a 50% volume of FBS. After mechanical agitation, the supernatant was transferred to coverslips coated with rat tail collagen I (Advanced Biomatrix; for imaging) or tissue culture plastic (for RNA analysis), and cells were allowed to adhere for 1 h. The media was then changed to Leibovitz's Media (L-15; Gibco) supplemented with 14.2 mM Hepes, pH 7.4, 10% FBS, and 1% antibiotic antimycotic for the remainder of the experiment. Pharmacological agents included CK666 (EMD Millipore), ML-7 (EMD Millipore), ROCKout (Santa Cruz Biotechology, Inc.), and BATI, a membrane-permeable MLCK inhibitor peptide (Totsukawa et al., 2004), which was synthesized by GenScript. Typically, four embryos were used for each coverslip, with all embryos for a given experiment performed on one day deriving from the same clutch. All experimental protocols were approved by the Stanford University Administrative Panel on Laboratory Animal Care under protocol no. 10240.

Genetic perturbations

Tol2/Multisite-Gateway technology (Kwan et al., 2007) was used to generate transgenic zebrafish expressing *hsp70:myosin light chain-mApple* or *actb1:EGFP-CAAX* as follows: To make *hsp70:myosin light chain-mApple*, we received the myosin light chain–mApple plasmid as a gift from M. Davidson (Florida State University, Tallahassee, FL). The myosin light chain-mApple construct was transferred into pME-MCS by restriction digest using EcoRI and HindIII, and then recombined with p5E-hsp70l promoter element, p3E-polyA polyadenylation signal, and pDestTol2pA2 vector backbone to produce *pTol2-hsp70l::myosin light chain-mApple*. To make *actb1:EGFP-CAAX*, we recombined the p5E-bactin1 promoter, pME-EGFPCAAX, and p3E-polyA polyadenylation signal with the pDestTol2pA2 vector backbone. The p5E-hsp70l, p5E-bactin1, pME-EGFPCAAX, p3E-polyA25, and pDestTol2pA2 Gateway entry vectors were gifts from C.-B. Chien (University of Utah, Salt Lake City, UT). Recombinations were performed using the Multi-site Gateway Three-Fragment Vector Construction kit (Invitrogen). 25 pg of each final pTol2 vector was coinjected at the one-cell stage with 25 pg transposase RNA synthesized with the SP6 mMessage mMachine kit (Ambion).

An antisense morpholino oligonucleotide (Gene Tools LLC) was designed to induce mis-splicing of exon 9 of im:7148400 and early termination of the transcript before its kinase domain. The morpholino (ACATACTTACACTCCTAGTTTCTCC) was resuspended in water at a stock concentration of 1 mM. 12 pg morpholino in a 1-nl volume was injected into embryos at the one-cell stage using standard procedures (Yuan and Sun, 2009). To check that mis-splicing occurs, RNA was extracted from individual embryos using the RNeasy Micro kit (QIAGEN). The following primers were used to amplify exons 8–10 (5′-3′): CAGCCAAGAGTCCCAGACAG, CTCTCTGTCCTTTGCCCGAC.

Microscopy

Live cells and fixed cells were imaged on an inverted microscope (Ti Eclipse; Nikon) at room temperature using a 40× NA 0.6 Plan Fluor air or a 100× NA 1.4 Plan-Apochromat oil objective lens (Nikon). All images were collected with a cooled back-thinned EM charge-coupled device (CCD) camera (iXon+ DU888; Andor Technology) with a 1× or 1.5× optivar using MicroManager 1.4 software. Live cells were imaged in their usual culture media. For cell tracks, a randomly selected region spanning a tiled series of 10 × 10 or 6 × 6 fields of view was imaged every minute for 20 min. For drug perturbation experiments, cells were imaged every 10 s for 10 min before drug addition, and continuing for 30 min after drug addition. For live-cell myosin experiments, cells were imaged every 3 s. Fixed cells were mounted in Vectashield mounting media (Vector Laboratories).

For 3D structured illumination microscopy experiments, fixed cells were mounted in SlowFade Gold mounting media (Invitrogen) and imaged on a DeltaVision OMX (GE Healthcare) microscope using DeltaVision software (GE Healthcare) with a 100× NA 1.4 UPlan-Apochromat oil objective lens (Olympus) using 0.125 µm z slices at room temperature. Images were collected with a cooled back-thinned EM-CCD camera (Evolve; Photometrics). 3D structured illumination reconstructions were created with the softWoRx imaging suite (GE Healthcare).

Cell trajectory analysis

Cells were tracked by hand using the MTrackJ plugin for ImageJ (National Institutes of Health). To calculate the decay rate of the velocity autocorrelation

for each track, the velocity autocorrelation was calculated and fit to a decaying exponential of the form $A \times e^{-kt}$. The fit was weighted by the square root of the number of observations at each time separation. The decay constant k was recorded for individual tracks and represented as a histogram (Fig. 1, g and h).

Cell shape analysis

Cell morphology was measured by representing cell shapes as polygons, as described previously (Pincus and Theriot, 2007; Barnhart et al., 2011). In brief, cell shapes were extracted either manually from phase images using Photoshop (Adobe) or by manually thresholding fluorescence images of cells expressing EGFPCAAX to produce binary images. Using Celltool, an open-source program for quantifying cell shape (Pincus and Theriot, 2007), cell contours were extracted from the binary images and then resampled at 200 evenly spaced points to generate the final polygons. To measure edge velocities, 200-point polygons were collected on long movies of individual cells. Point correspondences from one frame to the next were assigned by rotating the contour numberings to globally minimize net displacement of the edge. The velocity of each contour point between every pair of frames was calculated by dividing the normal component of the displacement vector for that contour point by the time interval at which the images were acquired.

Edge width, lifetime, and lateral propagation rates were then calculated from the resulting edge velocity maps (Fig. S1). To measure edge width, edge velocities for all contour points at a given point in time were extracted, and contiguous regions having a positive edge velocity were identified using custom MATLAB code. The length of these contiguous regions was then converted from contour points to microns using the circumference of the cell. To measure edge lifetime, edge velocity traces for a given contour point over time were extracted. Contiguous regions having a positive edge velocity were identified using custom MATLAB code and recorded as the lifetime for that particular protrusion cycle for that contour point. To measure the mean lateral propagation rate, we used the 2D Fourier transform to identify spatial frequencies present in edge velocity maps for individual cells. Peaks with amplitudes of at least half of the maximum amplitude detected were considered represented frequencies, which were then converted to lateral propagation rates.

Immunofluorescence and phalloidin staining

Indirect immunofluorescence for myosin was performed using polyclonal rabbit anti-pS19 myosin light chain antibody (ab2480; Abcam) at 1:100 dilution and a mouse monoclonal phospho-tyrosine antibody at 1:100 (#9411; Cell Signaling Technology). Cells were fixed in 4% formaldehyde in 0.32 M sucrose in PBS for 15 min, permeabilized with 0.5% Triton X-100 for 10 min, and blocked with PBS-BT (3% BSA, 0.1% Triton X-100, and 0.02% sodium azide) for 30 min before incubation with primary antibody diluted in PBS-BT. F-actin was labeled with 0.2 µM fluorescently conjugated phalloidin (Molecular Probes). To quantify total F-actin, we normalized total fluorescence by cell area. To quantify F-actin at protruding edges, we measured mean phalloidin intensity at manually selected swaths spanning 1 µm from the cell edge.

Membrane tension measurements

Tethers were pulled using a Bruker Catalyst AFM controlled by custom-made LabVIEW software mounted on an inverted fluorescent microscope (Carl Zeiss). Approach velocity was set to 1 µm/s, contact force to 100–500 pN, contact time to 5–10 s, and retraction speed to 10 µm/s. After a tether was pulled, the cantilever position was kept constant until it broke. A mean of 3.75 tethers were pulled for each cell. Resulting force–time curves were analyzed with the Kerssemakers algorithm (Kerssemakers et al., 2006) provided by J. Kerssemakers (Kavli Institute of Nanoscience, Delft University of Technology, Netherlands) in MATLAB. Cells were located by bright-field microscopy and the cantilever was positioned over the nucleus for tether measurement.

Olympus BioLevers (k = 60 pN/nm) were calibrated using the thermal noise method, plasma-cleaned for 30 s, and incubated in 4 mg/ml Concanavalin A (Sigma-Aldrich) for 2 h at 30°C. Before the measurements, cantilevers were rinsed in DPBS. For the measurement, cells were seeded on a glass slide in a home-built chamber filled with L15 cell culture medium supplemented with 3% FBS and not used longer than 1 h for data acquisition.

Note that the tether force values we measured are higher than those measured for adult cichlid keratocytes using a different method (Lieber et al., 2013). We confirmed that our method reproduces the values for cichlids as previously published.

Gene expression analysis

RNA was extracted from ∼1 × 10^5 keratocytes per sample using TRIzol (Invitrogen). Three biological replicates were collected for each developmental stage. Ribosomal RNA was depleted using the Ribo-Zero magnetic kit (Epicentre). The remaining mRNA was then fragmented with 8 min of incubation in 50 mM sodium carbonate/bicarbonate and 1 mM EDTA, pH 9.2, at 95°C. To prepare cDNA, first strand synthesis was performed with Superscript III (Invitrogen) using random hexamer priming, and second strand synthesis was performed with DNA Polymerase I (NEB). Illumina libraries were prepared from the cDNA in an automated fashion using the Illumina TruSeq sample prep kit with TruSeq adapters on an SPRIworks System I (Beckman Coulter). Sequencing reactions were performed on an Illumina Genome Analyzer IIX according to the manufacturer's instructions to generate 40-nt single-ended reads. All sequencing data were deposited in the NCBI Sequence Read Archive under accession no. SRP045504. On average, ∼20 million reads were collected per sample, and ∼70% of those reads were successfully mapped to the genome. Differential gene expression analysis was performed with the Tuxedo suite of gene expression analysis tools (Trapnell et al., 2012) using Ensembl Zv9 release 74 annotations. KEGG pathway gene sets for "Regulation of Actin Cytoskeleton" and "Focal Adhesion" were used to filter gene expression for cytoskeleton-related genes.

For qRT-PCR experiments, RNA was extracted from cells using the procedure in the previous paragraph, and cDNA was synthesized using the Superscript III First Strand Synthesis System (Invitrogen). qRT-PCR was performed using SYBR Select Master Mix (Invitrogen) on a StepOnePlus instrument (Applied Biosystems). The following primers were used (5′–3′):CAGCCAAGAGTCCCAGACAG,GGCCAAACTTCCCTACTCCT (*im:7148400*); CGAGCAGGAGATGGGAACC, CAACGGAAACGCTCATTGC (*bactin1*); TTGAGAAGAAAATCGGTGGTGCTG, GGAACGGTGTGATTGAGGGAAATTC (*ef1a*); GTCCCGAAAGGCTCCACTC, CCTCCGCTTTCCTCTCATTCAG (*g6pd*); and ATAAAAGTCGAGTGTGAGAGCGT, GCCTGACCAACGTGGATAGAG (*tuba1*). For relative quantification of *im:7148400* expression, we normalized to the geometric mean of four reference genes: *bactin1*, *ef1a*, *g6pd*, and *tuba1* (Hellemans et al., 2007).

Myosin texture analysis

Image entropy was used to quantify texture in local 21-pixel-diameter image regions using the entropyfilt function in MATLAB. Celltool was used to generate cell contours resampled at 200 points and to compute the mean image entropy in a 3-µm swath behind the leading edge for each of those points. Local image entropy was then correlated with edge velocity. For each contour position, protrusion-to-retraction transitions could be identified along with the texture values corresponding to that transition. All protrusion-to-retraction transitions were aligned with respect to retraction onset to show mean texture dynamics. Kymographs were made using the "Reslice" tool in ImageJ.

Statistical methods

The nonparametric Wilcoxon rank sum test was used for all data not passing the Jarque-Bera test for normality. Otherwise, two-tailed Student's *t* tests were used, assuming equal variance when the data passed the F-test for equal variance.

Online supplemental material

Fig. S1 illustrates how protrusion width, lifetime, and lateral propagation are calculated from an edge velocity map. Fig. S2 shows that the branching/capping ratio and cell size do not determine protrusion width. Fig. S3 shows individual correlations between protrusion width and protrusion lifetime or lateral propagation rate. Fig. S4 shows that Y-27632 has no effect on zebrafish keratocytes. Fig. S5 shows that ROCKout treatment does not affect protrusion width or lifetime, or lamellipodial accumulation of myosin. Video 1 provides an example of 2-dpf and 4-dpf keratocyte behavior. Video 2 shows how 2-dpf and 4-dpf cells recover from 10% DMSO-induced actin depolymerization. Video 3 shows a 4-dpf cell upon treatment with 25 µM ML7. Videos 4 and 5 show myosin dynamics in a representative 4-dpf multiple-front cell before and after ML7 treatment, respectively. Supplemental file 1 provides code to measure protrusion width, velocity, lifetime, and lateral propagation rate given an edge velocity matrix, as described in Fig. S1. Online supplemental material is available at http://www.jcb.org/cgi/content/full/jcb.201409001/DC1.

We are grateful to W. Talbot and members of the Talbot laboratory for zebrafish training and access to their fish facility, E. Barnhart for sharing edge velocity calculation code, and C.-B. Chien and M. Davidson for constructs.

We would also like to thank E. Barnhart, A. Mogilner, K. Keren, M. Rengarajan, S. Collins, and M. Chung for critical reading of the manuscript.

RNA sequencing was performed at the Stanford Functional Genomics Facility. Use of the OMX 3D SIM microscope was provided through the Stanford Cell Sciences Imaging Facility and partially funded by award no. 1S10OD01227601 from the National Center for Research Resources. This work was supported by the Stanford Medical Scientist Training Program National Institutes of Health (NIH) T32GM007365 (to S.S. Lou), the Damon Runyon Cancer Research Foundation (to A. Diz-Muñoz), NIH GM084040 (to O.D. Weiner), NIH GM074751 (to D.A. Fletcher), and the Howard Hughes Medical Institute (to J.A. Theriot).

The authors declare no competing financial interests.

Submitted: 1 September 2014
Accepted: 17 March 2015

References

Allard, J., and A. Mogilner. 2013. Traveling waves in actin dynamics and cell motility. *Curr. Opin. Cell Biol.* 25:107–115. http://dx.doi.org/10.1016/j.ceb.2012.08.012

Barnhart, E.L., K.-C. Lee, K. Keren, A. Mogilner, and J.A. Theriot. 2011. An adhesion-dependent switch between mechanisms that determine motile cell shape. *PLoS Biol.* 9:e1001059. http://dx.doi.org/10.1371/journal.pbio.1001059

Burnette, D.T., S. Manley, P. Sengupta, R. Sougrat, M.W. Davidson, B. Kachar, and J. Lippincott-Schwartz. 2011. A role for actin arcs in the leading-edge advance of migrating cells. *Nat. Cell Biol.* 13:371–382. http://dx.doi.org/10.1038/ncb2205

Burnette, D.T., L. Shao, C. Ott, A.M. Pasapera, R.S. Fischer, M.A. Baird, C. Der Loughian, H. Delanoe-Ayari, M.J. Paszek, M.W. Davidson, et al. 2014. A contractile and counterbalancing adhesion system controls the 3D shape of crawling cells. *J. Cell Biol.* 205:83–96. http://dx.doi.org/10.1083/jcb.201311104

Cai, Y., N. Biais, G. Giannone, M. Tanase, G. Jiang, J.M. Hofman, C.H. Wiggins, P. Silberzan, A. Buguin, B. Ladoux, and M.P. Sheetz. 2006. Nonmuscle myosin IIA-dependent force inhibits cell spreading and drives F-actin flow. *Biophys. J.* 91:3907–3920. http://dx.doi.org/10.1529/biophysj.106.084806

Cai, Y., O. Rossier, N.C. Gauthier, N. Biais, M.-A. Fardin, X. Zhang, L.W. Miller, B. Ladoux, V.W. Cornish, and M.P. Sheetz. 2010. Cytoskeletal coherence requires myosin-IIA contractility. *J. Cell Sci.* 123:413–423. http://dx.doi.org/10.1242/jcs.058297

Chew, T.-L., W.A. Wolf, P.J. Gallagher, F. Matsumura, and R.L. Chisholm. 2002. A fluorescent resonant energy transfer-based biosensor reveals transient and regional myosin light chain kinase activation in lamella and cleavage furrows. *J. Cell Biol.* 156:543–553. http://dx.doi.org/10.1083/jcb.200110161

Euteneuer, U., and M. Schliwa. 1984. Persistent, directional motility of cells and cytoplasmic fragments in the absence of microtubules. *Nature*. 310:58–61. http://dx.doi.org/10.1038/310058a0

Even-Ram, S., A.D. Doyle, M.A. Conti, K. Matsumoto, R.S. Adelstein, and K.M. Yamada. 2007. Myosin IIA regulates cell motility and actomyosin-microtubule crosstalk. *Nat. Cell Biol.* 9:299–309. http://dx.doi.org/10.1038/ncb1540

Giannone, G., B.J. Dubin-Thaler, H.-G. Döbereiner, N. Kieffer, A.R. Bresnick, and M.P. Sheetz. 2004. Periodic lamellipodial contractions correlate with rearward actin waves. *Cell*. 116:431–443. http://dx.doi.org/10.1016/S0092-8674(04)00058-3

Goodrich, H.B. 1924. Cell behavior in tissue cultures. *Biol. Bull.* 46:252–262. http://dx.doi.org/10.2307/1536726

Grimm, H.P., A.B. Verkhovsky, A. Mogilner, and J.J. Meister. 2003. Analysis of actin dynamics at the leading edge of crawling cells: implications for the shape of keratocyte lamellipodia. *Eur. Biophys. J.* 32:563–577. http://dx.doi.org/10.1007/s00249-003-0300-4

Hellemans, J., G. Mortier, A. De Paepe, F. Speleman, and J. Vandesompele. 2007. qBase relative quantification framework and software for management and automated analysis of real-time quantitative PCR data. *Genome Biol.* 8:R19. http://dx.doi.org/10.1186/gb-2007-8-2-r19

Houk, A.R., A. Jilkine, C.O. Mejean, R. Boltyanskiy, E.R. Dufresne, S.B. Angenent, S.J. Altschuler, L.F. Wu, and O.D. Weiner. 2012. Membrane tension maintains cell polarity by confining signals to the leading edge during neutrophil migration. *Cell*. 148:175–188. http://dx.doi.org/10.1016/j.cell.2011.10.050

Howe, K., M.D. Clark, C.F. Torroja, J. Torrance, C. Berthelot, M. Muffato, J.E.J. Collins, S. Humphray, K. McLaren, L. Matthews, et al. 2013. The zebrafish reference genome sequence and its relationship to the human genome. *Nature*. 496:498–503. (published erratum appears in *Nature*. 2014. 505:248) http://dx.doi.org/10.1038/nature12111

Keren, K., Z. Pincus, G.M. Allen, E.L. Barnhart, G. Marriott, A. Mogilner, and J.A. Theriot. 2008. Mechanism of shape determination in motile cells. *Nature*. 453:475–480. http://dx.doi.org/10.1038/nature06952

Kerssemakers, J.W.J., E.L. Munteanu, L. Laan, T.L. Noetzel, M.E. Janson, and M. Dogterom. 2006. Assembly dynamics of microtubules at molecular resolution. *Nature*. 442:709–712. http://dx.doi.org/10.1038/nature04928

Kwan, K.M., E. Fujimoto, C. Grabher, B.D. Mangum, M.E. Hardy, D.S. Campbell, J.M. Parant, H.J. Yost, J.P. Kanki, and C.-B. Chien. 2007. The Tol2kit: a multisite gateway-based construction kit for Tol2 transposon transgenesis constructs. *Dev. Dyn.* 236:3088–3099. http://dx.doi.org/10.1002/dvdy.21343

Lacayo, C.I., Z. Pincus, M.M. VanDuijn, C.A. Wilson, D.A. Fletcher, F.B. Gertler, A. Mogilner, and J.A. Theriot. 2007. Emergence of large-scale cell morphology and movement from local actin filament growth dynamics. *PLoS Biol.* 5:e233. http://dx.doi.org/10.1371/journal.pbio.0050233

Lawson, N.D., and S.A. Wolfe. 2011. Forward and reverse genetic approaches for the analysis of vertebrate development in the zebrafish. *Dev. Cell*. 21:48–64. http://dx.doi.org/10.1016/j.devcel.2011.06.007

Lee, J., A. Ishihara, J.A. Theriot, and K. Jacobson. 1993. Principles of locomotion for simple-shaped cells. *Nature*. 362:167–171. http://dx.doi.org/10.1038/362167a0

Le Guellec, D., G. Morvan-Dubois, and J.-Y. Sire. 2004. Skin development in bony fish with particular emphasis on collagen deposition in the dermis of the zebrafish (*Danio rerio*). *Int. J. Dev. Biol.* 48:217–231. http://dx.doi.org/10.1387/ijdb.15272388

Li, Z., X. Dong, Z. Wang, W. Liu, N. Deng, Y. Ding, L. Tang, T. Hla, R. Zeng, L. Li, and D. Wu. 2005. Regulation of PTEN by Rho small GTPases. *Nat. Cell Biol.* 7:399–404. (published erratum appears in *Nat. Cell Biol.* 2005. 7:531 and *Nat. Cell Biol*. 2006. 8:1038) http://dx.doi.org/10.1038/ncb1236

Lieber, A.D., S. Yehudai-Resheff, E.L. Barnhart, J.A. Theriot, and K. Keren. 2013. Membrane tension in rapidly moving cells is determined by cytoskeletal forces. *Curr. Biol.* 23:1409–1417. http://dx.doi.org/10.1016/j.cub.2013.05.063

Machacek, M., and G. Danuser. 2006. Morphodynamic profiling of protrusion phenotypes. *Biophys. J.* 90:1439–1452. http://dx.doi.org/10.1529/biophysj.105.070383

Mseka, T., and L.P. Cramer. 2011. Actin depolymerization-based force retracts the cell rear in polarizing and migrating cells. *Curr. Biol.* 21:2085–2091. http://dx.doi.org/10.1016/j.cub.2011.11.006

Murrell, M.P., and M.L. Gardel. 2012. F-actin buckling coordinates contractility and severing in a biomimetic actomyosin cortex. *Proc. Natl. Acad. Sci. USA*. 109:20820–20825. http://dx.doi.org/10.1073/pnas.1214753109

Nolen, B.J., N. Tomasevic, A. Russell, D.W. Pierce, Z. Jia, C.D. McCormick, J. Hartman, R. Sakowicz, and T.D. Pollard. 2009. Characterization of two classes of small molecule inhibitors of Arp2/3 complex. *Nature*. 460:1031–1034. http://dx.doi.org/10.1038/nature08231

Ofer, N., A. Mogilner, and K. Keren. 2011. Actin disassembly clock determines shape and speed of lamellipodial fragments. *Proc. Natl. Acad. Sci. USA*. 108:20394–20399. http://dx.doi.org/10.1073/pnas.1105333108

Ohta, Y., J.H. Hartwig, and T.P. Stossel. 2006. FilGAP, a Rho- and ROCK-regulated GAP for Rac binds filamin A to control actin remodelling. *Nat. Cell Biol.* 8:803–814. http://dx.doi.org/10.1038/ncb1437

Pincus, Z., and J.A. Theriot. 2007. Comparison of quantitative methods for cell-shape analysis. *J. Microsc.* 227:140–156. http://dx.doi.org/10.1111/j.1365-2818.2007.01799.x

Ponti, A., M. Machacek, S.L. Gupton, C.M. Waterman-Storer, and G. Danuser. 2004. Two distinct actin networks drive the protrusion of migrating cells. *Science*. 305:1782–1786. http://dx.doi.org/10.1126/science.1100533

Ryan, G.L., N. Watanabe, and D. Vavylonis. 2012. A review of models of fluctuating protrusion and retraction patterns at the leading edge of motile cells. *Cytoskeleton (Hoboken)*. 69:195–206. http://dx.doi.org/10.1002/cm.21017

Saitoh, M., T. Ishikawa, S. Matsushima, M. Naka, and H. Hidaka. 1987. Selective inhibition of catalytic activity of smooth muscle myosin light chain kinase. *J. Biol. Chem.* 262:7796–7801.

Schramek, D., A. Sendoel, J.P. Segal, S. Beronja, E. Heller, D. Oristian, B. Reva, and E. Fuchs. 2014. Direct in vivo RNAi screen unveils myosin IIa as a tumor suppressor of squamous cell carcinomas. *Science*. 343:309–313. http://dx.doi.org/10.1126/science.1248627

Svitkina, T.M., A.B. Verkhovsky, K.M. McQuade, and G.G. Borisy. 1997. Analysis of the actin-myosin II system in fish epidermal keratocytes: mechanism of cell body translocation. *J. Cell Biol.* 139:397–415. http://dx.doi.org/10.1083/jcb.139.2.397

Totsukawa, G., Y. Wu, Y. Sasaki, D.J. Hartshorne, Y. Yamakita, S. Yamashiro, and F. Matsumura. 2004. Distinct roles of MLCK and ROCK in the regulation of membrane protrusions and focal adhesion dynamics during cell migration of fibroblasts. *J. Cell Biol.* 164:427–439. http://dx.doi.org/10.1083/jcb.200306172

Trapnell, C., A. Roberts, L. Goff, G. Pertea, D. Kim, D.R. Kelley, H. Pimentel, S.L. Salzberg, J.L. Rinn, and L. Pachter. 2012. Differential gene and transcript expression analysis of RNA-seq experiments with TopHat and Cufflinks. *Nat. Protoc.* 7:562–578. http://dx.doi.org/10.1038/nprot.2012.016

Tsai, F.-C., and T. Meyer. 2012. Ca^{2+} pulses control local cycles of lamellipodia retraction and adhesion along the front of migrating cells. *Curr. Biol.* 22:837–842. http://dx.doi.org/10.1016/j.cub.2012.03.037

Verkhovsky, A.B., T.M. Svitkina, and G.G. Borisy. 1995. Myosin II filament assemblies in the active lamella of fibroblasts: their morphogenesis and role in the formation of actin filament bundles. *J. Cell Biol.* 131:989–1002. http://dx.doi.org/10.1083/jcb.131.4.989

Vicente-Manzanares, M., J. Zareno, L. Whitmore, C.K. Choi, and A.F. Horwitz. 2007. Regulation of protrusion, adhesion dynamics, and polarity by myosins IIA and IIB in migrating cells. *J. Cell Biol.* 176:573–580. http://dx.doi.org/10.1083/jcb.200612043

Vicente-Manzanares, M., M.A. Koach, L. Whitmore, M.L. Lamers, and A.F. Horwitz. 2008. Segregation and activation of myosin IIB creates a rear in migrating cells. *J. Cell Biol.* 183:543–554. http://dx.doi.org/10.1083/jcb.200806030

Vicente-Manzanares, M., K. Newell-Litwa, A.I. Bachir, L.A. Whitmore, and A.R. Horwitz. 2011. Myosin IIA/IIB restrict adhesive and protrusive signaling to generate front-back polarity in migrating cells. *J. Cell Biol.* 193:381–396. http://dx.doi.org/10.1083/jcb.201012159

Vogel, S.K., Z. Petrasek, F. Heinemann, and P. Schwille. 2013. Myosin motors fragment and compact membrane-bound actin filaments. *eLife*. 2:e00116. http://dx.doi.org/10.7554/eLife.00116

Wang, H.-R., Y. Zhang, B. Ozdamar, A.A. Ogunjimi, E. Alexandrova, G.H. Thomsen, and J.L. Wrana. 2003. Regulation of cell polarity and protrusion formation by targeting RhoA for degradation. *Science*. 302:1775–1779. http://dx.doi.org/10.1126/science.1090772

Weiser, D.C., and D. Kimelman. 2012. Analysis of cell shape and polarity during zebrafish gastrulation. *Methods Mol. Biol.* 839:53–68. http://dx.doi.org/10.1007/978-1-61779-510-7_5

Wessels, D., D.R. Soll, D. Knecht, W.F. Loomis, A. De Lozanne, and J. Spudich. 1988. Cell motility and chemotaxis in *Dictyostelium* amebae lacking myosin heavy chain. *Dev. Biol.* 128:164–177. http://dx.doi.org/10.1016/0012-1606(88)90279-5

Westerfield, M. 2007. The Zebrafish Book, 5th Edition; A Guide for the Laboratory Use of Zebrafish (Danio rerio). University of Oregon Press, Eugene, OR. 396 pp.

Wilson, C.A., M.A. Tsuchida, G.M. Allen, E.L. Barnhart, K.T. Applegate, P.T. Yam, L. Ji, K. Keren, G. Danuser, and J.A. Theriot. 2010. Myosin II contributes to cell-scale actin network treadmilling through network disassembly. *Nature*. 465:373–377. http://dx.doi.org/10.1038/nature08994

Wong, K., O. Pertz, K. Hahn, and H. Bourne. 2006. Neutrophil polarization: spatiotemporal dynamics of RhoA activity support a self-organizing mechanism. *Proc. Natl. Acad. Sci. USA*. 103:3639–3644. http://dx.doi.org/10.1073/pnas.0600092103

Worthylake, R.A., and K. Burridge. 2003. RhoA and ROCK promote migration by limiting membrane protrusions. *J. Biol. Chem.* 278:13578–13584. http://dx.doi.org/10.1074/jbc.M211584200

Xu, J., F. Wang, A. Van Keymeulen, P. Herzmark, A. Straight, K. Kelly, Y. Takuwa, N. Sugimoto, T. Mitchison, and H.R. Bourne. 2003. Divergent signals and cytoskeletal assemblies regulate self-organizing polarity in neutrophils. *Cell*. 114:201–214. http://dx.doi.org/10.1016/S0092-8674(03)00555-5

Xu, J., X.-P. Gao, R. Ramchandran, Y.-Y. Zhao, S.M. Vogel, and A.B. Malik. 2008. Nonmuscle myosin light-chain kinase mediates neutrophil transmigration in sepsis-induced lung inflammation by activating β_2 integrins. *Nat. Immunol.* 9:880–886. http://dx.doi.org/10.1038/ni.1628

Yam, P.T., C.A. Wilson, L. Ji, B. Hebert, E.L. Barnhart, N.A. Dye, P.W. Wiseman, G. Danuser, and J.A. Theriot. 2007. Actin-myosin network reorganization breaks symmetry at the cell rear to spontaneously initiate polarized cell motility. *J. Cell Biol.* 178:1207–1221. http://dx.doi.org/10.1083/jcb.200706012

Yarrow, J.C., G. Totsukawa, G.T. Charras, and T.J. Mitchison. 2005. Screening for cell migration inhibitors via automated microscopy reveals a Rho-kinase inhibitor. *Chem. Biol.* 12:385–395. http://dx.doi.org/10.1016/j.chembiol.2005.01.015

Yuan, S., and Z. Sun. 2009. Microinjection of mRNA and morpholino antisense oligonucleotides in zebrafish embryos. *J. Vis. Exp.* 27–29.